An adaptive metamaterial beam with hybrid shunting circuits for extremely broadband control of flexural waves

2016 Smart Mater. Struct. 25 105036

(http://iopscience.iop.org/0964-1726/25/10/105036)

IOP Publishing Smart Materials and Structures
Smart Mater. Struct. 25 (2016) 105036 (13pp) doi:10.1088/0964-1726/25/10/105036

An adaptive metamaterial beam with hybrid shunting circuits for extremely broadband control of flexural waves

Y Y Chen[1], G K Hu[2] and G L Huang[1]

[1] Department of Mechanical and Aerospace Engineering, University of Missouri, Columbia, MO, 65211, USA
[2] School of Aerospace Engineering, Beijing Institute of Technology, Beijing, People's Republic of China

E-mail: huangg@missouri.edu

Received 19 June 2016, revised 5 August 2016
Accepted for publication 30 August 2016
Published 26 September 2016

Abstract

A great deal of research has been devoted to controlling the dynamic behaviors of phononic crystals and metamaterials by directly tuning the frequency regions and/or widths of their inherent band gaps. Here, we report a new class of adaptive metamaterial beams with hybrid shunting circuits to realize super broadband Lamb-wave band gaps at an extreme subwavelength scale. The proposed metamaterial is made of a homogeneous host beam on which tunable local resonators consisting of hybrid shunted piezoelectric stacks with proof masses are attached. The hybrid shunting circuits are composed of negative-capacitance and negative-inductance elements connected in series or in parallel in order to tune the desired frequency-dependent stiffness. It is shown theoretically and numerically that by properly modifying the shunting impedance, the adaptive mechanical mechanism within the tunable resonator can produce high-pass and low-pass wave filtering capabilities for the zeroth-order anti-symmetric Lamb-wave modes. These unique behaviors are due to the hybrid effects from the negative-capacitance and negative-inductance circuit elements. Such a system opens up important perspectives for the development of adaptive vibration or wave-attenuation devices for broadband frequency applications.

Keywords: adaptive metamaterials, broadband, guided wave control

(Some figures may appear in colour only in the online journal)

1. Introduction

Inspired by their electromagnetic counterparts, acoustic metamaterials have recently been developed with various application potentials and have become an active field [1–3]. At the same time, elastic/mechanical metamaterials have also received a great deal of attention due to the unusual properties and unprecedented dynamic behaviors that they exhibit. Their unique dynamic features are a result of coupled elastic wave scattering, in most instances, with internally resonating units (metastructures). By tailoring the metastructure at a sub-wavelength scale, elastic/mechanical metamaterials gain the ability to suppress or significantly absorb elastic waves with minimal impact on their overall weight and size. This unlocks opportunities for controlling low-frequency wave propagation without the need to scale the structures to unmanageable sizes [4–8]. However, the narrow resonant stop bands of the existing elastic/mechanical metamaterials strictly limit their use for various noise and/or vibration absorption applications because most engineering problems are broadband in nature. Moreover, actively controlling the position and width of the band-gap frequency region in real-time is very difficult in practice, if not impossible, for passive metamaterials. One of the most pronounced challenges in elastic/mechanical metamaterial development is the ability to tune their performance in an adaptive manner without requiring physical microstructural modifications.

The piezoelectric shunting technique was originally proposed by Forward [9] and further investigated by Hagood and Von Flotow [10], who developed the first analytical formulation to demonstrate how the equivalent material properties of a piezoelectric patch are altered by passive shunting networks.

Therefore, the introduction of shunted piezoelectric materials into the metastructures' building blocks has great potential to allow for tuning of the effective properties of the metastructures [11]. Airoldi and Ruzzene [12] designed a one-dimensional (1D) tunable acoustic metamaterial by using a simple elastic beam fitted with a periodic array of piezoelectric patches whose electrodes are connected to resistive-inductive (RL) shunted circuits. It was demonstrated that the tunable characteristics of the shunting circuits allowed the equivalent mechanical impedance to be tuned so that band gaps could be generated over desired frequency ranges without any modifications to the elastic structures. Two-dimensional (2D) periodic arrays of resonant shunted piezoelectric patches have also been used to achieve tunable acoustic metamaterial waveguides [13, 14]. The resonant characteristics of the shunting current lead to strong attenuation and negative group velocities at frequencies controlled by the electrical impedance. However, the resonant band gaps produced in these phononic metacomposites with passive RL shunting networks are usually very narrow.

In order to achieve vibration and/or wave attenuations at broadband frequencies, piezoelectric patches with multi-branch resonant shunting circuits have been investigated [15]. In addition, the active negative-capacitive shunting technique was found to be an effective method to broaden the attenuation frequency region. Beck *et al* [16] experimentally demonstrated that a periodic array of piezoelectric patches shunted with negative-capacitance circuits can suppress broadband flexural vibrations of a cantilever beam. Collet *et al* [17] developed a numerical approach for modeling and optimizing 2D smart metacomposites with shunted piezoelectric patches. More recently, periodic arrays of hybrid-circuit shunted piezoelectric patches were used to broaden the Bragg band gaps presented in phononic beams [18]. However, the vibration and/or wave-attenuation abilities due to electrical damping are usually weaker than the mechanical resonant damping. Therefore, Chen *et al* [19] implemented the negative-capacitance piezoelectric shunting technique into metastructures to actively tune the locally resonant frequencies of mechanical resonators by modifying the stiffness of the resonant microstructure, in order to control the band-gap region of the active elastic/mechanical metamaterial. Following this concept, Zhu *et al* [20] designed an adaptive elastic metamaterial, where harmonic vibration testing as well as transient wave-propagation tests were conducted on the fabricated metamaterial sample to illustrate their tunable vibration suspension and elastic wave-attenuation abilities. However, actively controlled band gaps with position and width variations are still narrow in real-time, which eventually cannot be used for broadband incident loadings.

In this paper, we consider a novel approach to significantly broaden the subwavelength band gaps of an adaptive metamaterial beam to extremely low- or high-frequency regions based on periodic arrays of local resonators with hybrid-circuit shunted piezoelectric stacks. The negative-capacitance and negative-inductance shunting circuits are connected to the same individual piezoelectric stack in series or in parallel. The complex band structure of the infinite periodic structure is predicted by the transfer matrix (TM) method, which is compared with the frequency-response function of a finite structure calculated by a multi-physics finite element (FE) method. Our analytical and numerical results demonstrate that hybrid shunting circuits can create super-wide band gaps to achieve high-pass and low-pass wave filtering by appropriately selecting the values of negative capacitance and negative inductance to adaptively tune the effective modulus of piezoelectric stacks. This design is very significant for the practical applications of low-frequency sound and structural vibration/wave attenuations in engineering.

2. The adaptive metamaterial beam and modeling methods

2.1. Microstructures of the adaptive metamaterial beam with hybrid shunting circuits

Figure 1(a) shows a schematic of the proposed adaptive metamaterial beam design, which is comprised of a host beam with periodically surface-bonded piezoelectric stacks with cylindrical proof masses on the stacks' top surfaces. Each of the piezoelectric stacks is made of several stacked rectangular piezoelectric plates for strong electromechanical coupling and is individually shunted with uniform hybrid circuits for modulus control. The employment of piezoelectric stacks instead of piezoelectric bars in the proposed microstructure can significantly enlarge the capacitance of the piezoelectric element and reduce the high voltage requirement in the modulus control, which offers great benefits in metamaterial applications. Specifically, two kinds of hybrid circuits, TYPE I and TYPE II circuits (shown on the right-hand side of figure 1(a)), are considered in the study for broadband low- and high-frequency wave attenuations, respectively. The TYPE I circuit is integrated with a negative capacitance C_1 and a negative inductance L_1 connected in series. The TYPE II circuit is constructed with a negative capacitance C_2 and a negative inductance L_2 connected in parallel. Both of the two kinds of hybrid circuits can be achieved with analog negative impedance circuits or digital synthetic impedance circuits. It should be noted that there is no theoretical power consumption within the shunting networks, because all the equivalent elements used in the circuits are capacitive and inductive. When the real circuits are built, the power consumption caused by the constitutive operational amplifiers, resistors and/or digital signal processors should be considered.

As also shown in figure 1(a) the side length and height of the piezoelectric stacks, as well as diameter and height of the cylindrical masses are denoted as a_p, h_p, d_m and h_m, respectively. The thickness of the host plate and lattice constant of the periodic metamaterial are represented by h_b and L_b, respectively. The width of the metamaterial beam is selected to be the same as the lattice constant. The main creativity of the current microstructure design is that the dimension of the piezoelectric stack with a relatively large height-to-width ratio is much smaller than the dimension of the proof mass. Therefore, the dominated deformation of the piezoelectric stack will be along

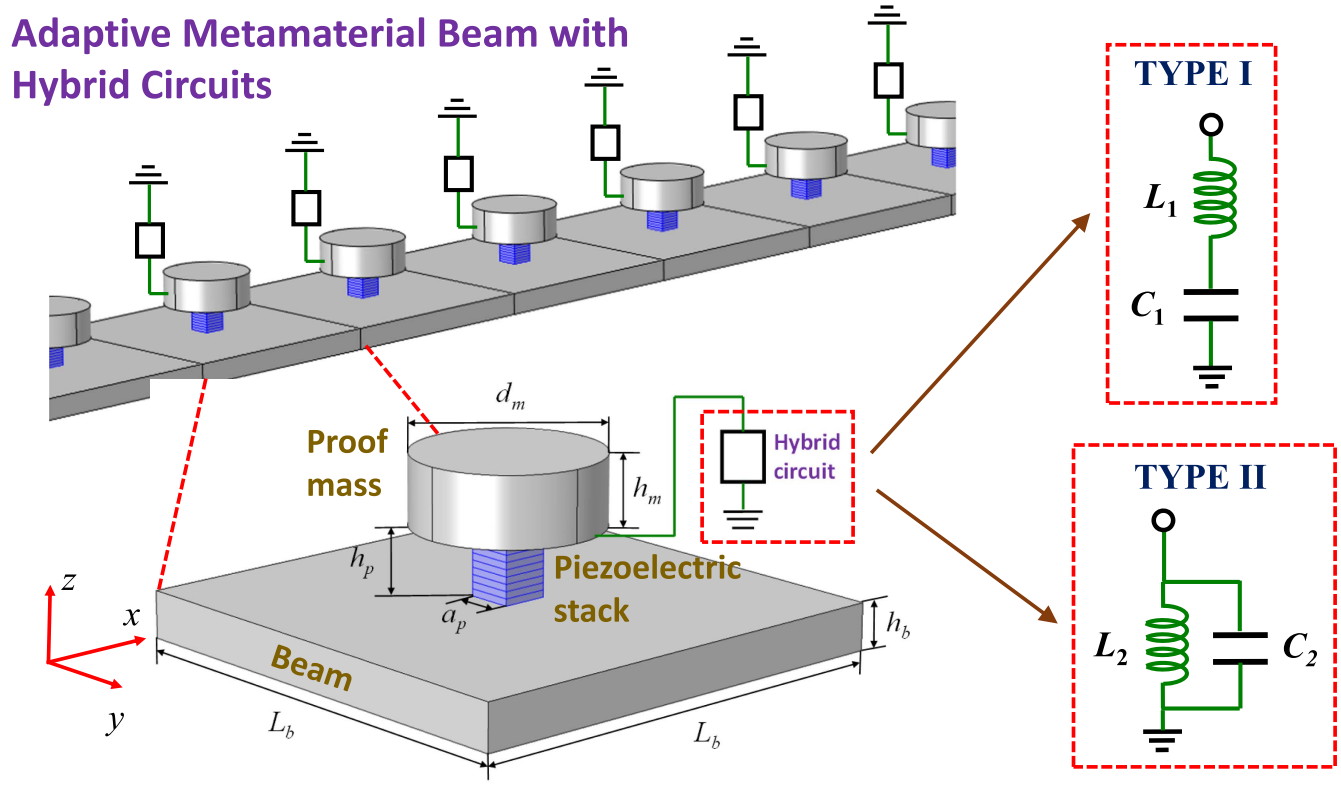

(a)

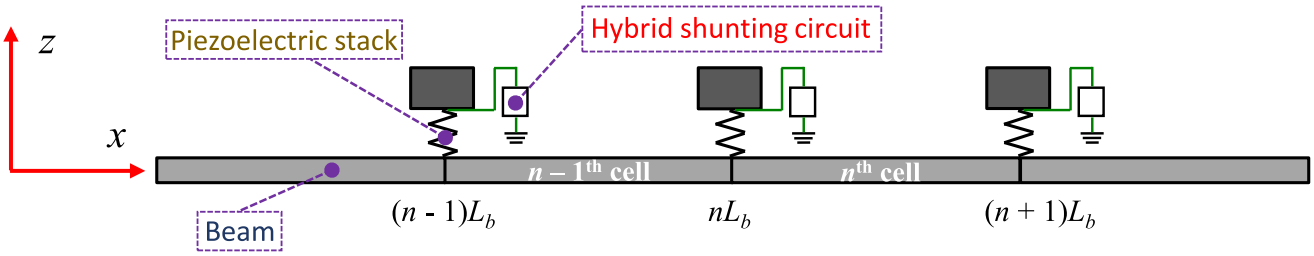

(b)

Figure 1. (a) Schematic of the adaptive metamaterial beam with piezoelectric stacks shunted by hybrid negative-capacitance and negative-inductance circuits; (b) Schematic of the 2D theoretical model of the adaptive metamaterial beam.

the z-direction as an effective mechanical connectivity (the object between the host beam and the attached resonator, which is quantitatively characterized by the effective modulus of the connected piezoelectric stack to describe the stress–strain correlation along the longitudinal direction), when the metamaterial beam is subjected to a flexural wave. As a result, the in-plane and out-of-plane coupling motions of the local resonators can be significantly minimized.

2.2. Modulus tuning of piezoelectric stacks shunted with hybrid circuits

According to the model by Hagood [10], both the storage and loss modulii of piezoelectric materials can be controlled by external electrical shunting networks. Based on this concept, the variation of the stiffness of piezoelectric stacks shunted with hybrid circuits is quantitatively characterized. Different from previous studies, which considered frequency-independent modulus variations by using negative capacitance [19], this study focuses on frequency-dependent modulus alterations in order to achieve extremely broadband wave control. Here, we consider a piezoelectric stack composed of N number of layers of piezoelectric plates with the same geometric dimensions. The polarization directions of each of the two adjacent individual plates are opposite in the stack design (being positive and negative z-directions or vice versa, respectively). In this study, the boundary effects from the interfaces between the stacks, host beam and proof masses are

ignored, due to the large height-to-width ratio of the piezoelectric stack used in the adaptive metamaterial design. The longitudinal deformation along the z-direction is assumed to be uniform within each of the stacks. Since all four side surfaces of the stack are traction- and charge-free, the in-plane stresses and electric fields in each of the individual piezoelectric plates are neglected. Based on these assumptions, the 3D piezoelectric constitutive equations can be reduced to two 1D equations for the piezoelectric plates with polarization directions along the positive z-direction as

$$S_{33} = d_{33}E_3 + s_{33}^E T_{33}, \tag{1a}$$

$$D_3 = \varepsilon_{33}^T E_3 + d_{33}T_{33}, \tag{1b}$$

where S_{33}, T_{33}, D_3 and E_3 denote the stress, strain, electric displacement and electric field along the z-direction, respectively, and s_{33}^E, d_{33} and ε_{33}^T represent the elastic compliance at constant electric field, piezoelectric coefficient and dielectric coefficient at constant stress of the piezoelectric material, respectively. By properly considering the electrical boundary conditions due to the shunting impedance Z_{sh}, the dynamic effective modulus of the piezoelectric stack can be obtained as [10]

$$E_p^{\text{eff}} = \frac{E_p^E}{1 - \dfrac{k_{33}^2}{1 + 1/(i\omega Z_{Sh} C_p^T)}}, \tag{2}$$

where $E_p^E = \dfrac{1}{s_{33}^E}$, $k_{33} = \sqrt{\dfrac{d_{33}^2 s_{33}^E}{\varepsilon_{33}^T}}$ and $C_p^T = \dfrac{N^2 a_p^2 \varepsilon_{33}^T}{h_p}$ are the short-circuit modulus, electromechanical coupling coefficient and the capacitance of the piezoelectric stack, respectively. According to equation (2), if the shunting impedance is not purely capacitive, the final effective modulus will be a function of both the shunting impedance and the working frequency. Specifically, for the TYPE I and TYPE II circuits, the shunting impedances can be expressed, respectively, as

$$Z_{\text{sh}}^{(1)} = \frac{1}{i\omega C_p^T \lambda_1} - \frac{i\omega}{\omega_{s1}^2 C_p^T}, \tag{3a}$$

$$Z_{\text{sh}}^{(2)} = \frac{1}{i\omega C_p^T \lambda_2 - \dfrac{\omega_{s2}^2 C_p^T}{i\omega}}, \tag{3b}$$

where $\lambda_i = \dfrac{C_i}{C_p^T}$ and $\omega_{si}^2 = \dfrac{1}{|L_i|\ C_p^T}$ with i being 1 or 2. Thus, by substituting equations (3a) and (3b) into equation (2), the equivalent modulus due to these two kinds of shunting circuits can be obtained.

2.3. Dispersion relations of the adaptive metamaterial beam

In order to characterize the unique wave-attenuation properties of the adaptive metamaterial beam, an analytical model based on the TM method is developed to consider effects from hybrid shunting circuits, which is shown in figure 1(b). In the model, a plane stress assumption is used for the metamaterial beam structure. For simplicity, the piezoelectric stacks are represented by linear springs with tunable stiffness $k_p = \dfrac{E_p^{\text{eff}} a_p^2}{h_p}$ controlled by the shunting circuits. The rotational and x-direction translational motions of the proof masses are ignored in the model. Based on the Timoshenko beam theory, the governing equation for the host beam can be written as [6]

$$\frac{E_b I_b}{\rho_b S_b}\frac{\partial^4 w}{\partial x^4} - \frac{I_b}{S_b}\left(1 + \frac{E_b}{\kappa_b G_b}\right)\frac{\partial^4 w}{\partial x^2 \partial t^2} + \frac{\partial^2 w}{\partial t^2} + \frac{\rho_b I_b}{\kappa_b G_b S_b}\frac{\partial^4 w}{\partial t^4} = 0, \tag{4}$$

where w denotes the out-of-plane displacement field on the neutral plane of the host beam.E_b, G_b, ρ_b, I_b, S_b, and κ_b are the Young's modulus, shear modulus, mass density, area moment of inertia, area of cross-section and Timoshenko shear coefficient of the host beam, respectively. In our analysis, we consider a harmonic solution to equation (4) as $w(x, t) = W(x)\exp(i\omega t)$, and the harmonic time terms are suppressed in the following equations. For the n-th unit cell, the general solution can be expressed as [6]

$$W_n(x_n) = A_n e^{\lambda_1 x_n} + B_n e^{\lambda_2 x_n} + C_n e_n^{\lambda_3 x_n} + D_n e^{\lambda_4 x_n}, \tag{5}$$

where $x_n = x - nL_b$, $nL_b \leqslant x \leqslant (n+1)L_b$, $\lambda_{1,2,3,4} = \pm\sqrt{\dfrac{\alpha \pm \sqrt{\alpha^2 + 4\beta}}{2}}$ with $\alpha = -\dfrac{\rho_b \omega^2}{E_b} - \dfrac{\rho_b \omega^2}{\kappa_b G_b}$ and $\beta = \dfrac{\rho_b S_b \omega^2}{E_b I_b} - \dfrac{\rho_b^2 \omega^4}{\kappa_b G_b E_b}$. The out-of-plane point force on the interface between the nth and $(n+1)$-th unit cell caused by the tunable resonator can be expressed as [6]

$$F_n = \frac{-\omega^2 m_r k_p W_n(0)}{-\omega^2 m_r + k_p}, \tag{6}$$

where m_r represents the weight of the cylindrical proof mass. Different from the previous TM method used in metamaterial beams [6], which considered boundary continuity conditions based on Euler beam assumptions, the currently developed TM method considers boundary continuity conditions based on Timoshenko beam theory, consistent with the governing equation. Thus, the continuity conditions of the displacement, total rotation angle of the cross-section, bending moment and shear force at the point, $x = nL_b$, require

$$W_n(0) = W_{n-1}(L_b), \tag{7a}$$

$$\psi_n(0) = \psi_{n-1}(L_b), \tag{7b}$$

$$E_b I_b \frac{\partial \psi_n(0)}{\partial x} = E_b I_b \frac{\partial \psi_{n-1}(L_b)}{\partial x}, \tag{7c}$$

$$\kappa_b G_b S_b\left(\frac{\partial W_n(0)}{\partial x} - \psi_n(0)\right) = \kappa_b G_b S_b \times \left(\frac{\partial W_{n-1}(L_b)}{\partial x} - \psi_{n-1}(L_b)\right) + F_n, \tag{7d}$$

where $\psi = \dfrac{\mathrm{d}W}{\mathrm{d}x} + \gamma$, with γ being the shear angle. Numerical simulations have been conducted in the example of the metamaterial beams [6], and it is found that the Timoshenko boundary conditions are necessary for correctly predicting

Table 1. Geometric and material parameters of the constitutive materials of the proposed adaptive material beam.

Geometric parameters (mm)			
L_b	7.5	h_m	5.0
h_b	2.0	h_p	3.0
d_m	5.0	a_p	1.0
Material properties (Steel)			
E_b	210.0 GPa	G_b	80.8 GPa
ρ_b	7800.0 kg m^{-3}		
Material properties (PMN-33%PT) [21]			
$c_{11}{}^E$	115.0 GPa	e_{15}	10.1 C m^{-2}
$c_{12}{}^E$	103.0 GPa	e_{31}	-3.9 C m^{-2}
$c_{13}{}^E$	102.0 GPa	e_{33}	20.3 C m^{-2}
$c_{33}{}^E$	103.0 GPa	d_{33}	2820.0 $\times$ 10^{-12} C N^{-1}
$c_{44}{}^E$	69.0 GPa	ε_{11}^S	1434.0ε_0
$c_{66}{}^E$	66.0 GPa	ε_{33}^S	680.0ε_0
$s_{33}{}^E$	119.6 $\times$ 10^{-12} m^2 N^{-1}	ε_{33}^T	8200.0ε_0

band structures of the metamaterial with larger thickness-to-lattice constant ratios and higher resonant frequency cases when the wavelength is comparable with the lattice constant of the metamaterial.

Substituting equations (5) and (6) into equation (7), one can obtain

$$\mathbf{K}\mathbf{A}_n = \mathbf{H}\mathbf{A}_{n-1}, \tag{8}$$

where

$$\mathbf{K} = \begin{bmatrix} 1 & 1 & 1 & 1 \\ a\lambda_1 + b\lambda_1^3 & a\lambda_2 + b\lambda_2^3 & a\lambda_3 + b\lambda_3^3 & a\lambda_4 + b\lambda_4^3 \\ a\lambda_1^2 + b\lambda_1^4 & a\lambda_2^2 + b\lambda_2^4 & a\lambda_3^2 + b\lambda_3^4 & a\lambda_4^2 + b\lambda_4^4 \\ \lambda_1 - \dfrac{F_n}{\kappa_b G_b S_b} & \lambda_2 - \dfrac{F_n}{\kappa_b G_b S_b} & \lambda_3 - \dfrac{F_n}{\kappa_b G_b S_b} & \lambda_4 - \dfrac{F_n}{\kappa_b G_b S_b} \end{bmatrix},$$

$$\mathbf{H} = \begin{bmatrix} e^{\lambda_1 L_b} & e^{\lambda_2 L_b} & e^{\lambda_3 L_b} & e^{\lambda_4 L_b} \\ (a\lambda_1 + b\lambda_1^3)e^{\lambda_1 L_b} & (a\lambda_2 + b\lambda_2^3)e^{\lambda_2 L_b} & (a\lambda_3 + b\lambda_3^3)e^{\lambda_3 L_b} & (a\lambda_4 + b\lambda_4^3)e^{\lambda_4 L_b} \\ (a\lambda_1^2 + b\lambda_1^4)e^{\lambda_1 L_b} & (a\lambda_2^2 + b\lambda_2^4)e^{\lambda_2 L_b} & (a\lambda_3^2 + b\lambda_3^4)e^{\lambda_3 L_b} & (a\lambda_4^2 + b\lambda_4^4)e^{\lambda_4 L_b} \\ \lambda_1 e^{\lambda_1 L_b} & \lambda_2 e^{\lambda_2 L_b} & \lambda_3 e^{\lambda_3 L_b} & \lambda_4 e^{\lambda_4 L_b} \end{bmatrix},$$

$$\mathbf{A}_n = [A_n \quad B_n \quad C_n \quad D_n]^T,$$

with

$$a = \frac{\kappa_b G_b E_b + \dfrac{\rho_b \omega^2 E_b I_b}{\kappa_b G_b}}{\kappa_b G_b E_b - \rho_b \omega^2 I_b},$$

$$b = \frac{E_b I_b}{\kappa_b G_b E_b - \rho_b \omega^2 I_b}.$$

Due to the periodicity of the metamaterial beam in the x-direction, the Bloch theorem guarantees

$$\mathbf{A}_n = \mathrm{e}^{\mathrm{i}k_x L_b}\mathbf{A}_{n-1}, \tag{9}$$

where k_x is the wave vector along the x-direction. By inserting equation (9) into equation (8), a standard eigenvalue problem is yielded as

$$|\mathbf{K}^{-1}\mathbf{H} - \mathrm{e}^{\mathrm{i}k_x L_b}\mathbf{I}| = 0, \tag{10}$$

where $\mathbf{I}$ is the 4×4 identity matrix. Finally, equation (10) illustrates the dispersion relations of the adaptive metamaterial beam with hybrid shunting circuits. Based on the given frequencies, the complex wavenumbers are determined, from which the wave-propagation properties are characterized.

3. Results and discussion

In this section, the complex band structure of the metamaterial beam with various effective modulii of the mechanical connectivity is characterized first. Based on the properties of the band-gap behaviors observed, two kinds of hybrid shunting circuits are designed to electronically realize the physical properties. The performance of the adaptive metamaterial beam utilizing these hybrid circuits is then examined by conducting multi-physics numerical simulations on a finite metamaterial beam to demonstrate extremely broadband attenuation capabilities.

3.1. Complex band structures of the metamaterial beam

As an illustrative example, we select steel for the material of the host beam and cylindrical proof masses. The piezoelectric stacks are made of PMN-33%PT single crystals, which usually have larger piezoelectric coefficients and are softer than the commonly used piezoelectric ceramic materials (PZT). As a result, the total controlling voltage due to

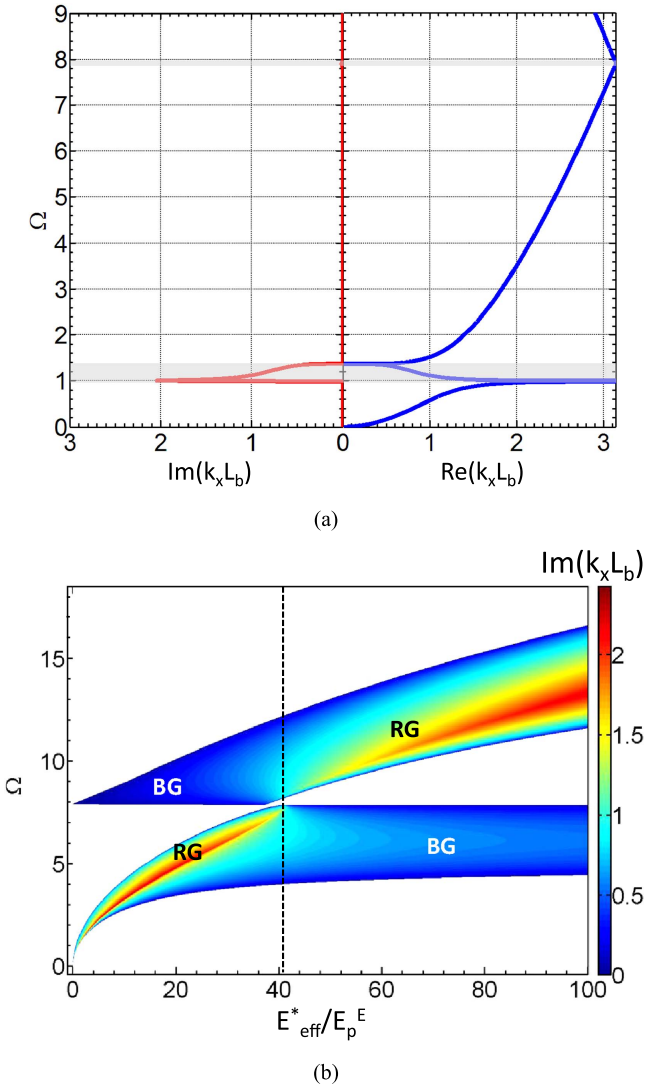

Figure 2. (a) Complex band structure of the adaptive metamaterial beam with short circuits; (b) Attenuation constant of flexural waves with different frequency-independent normalized effective modulii of the mechanical connectivity.

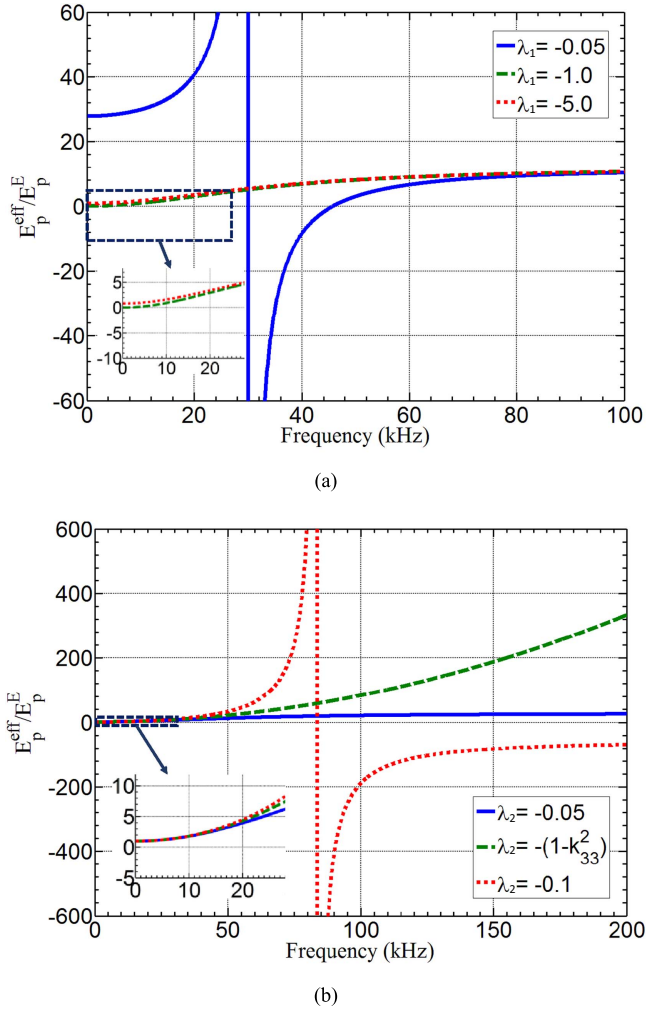

Figure 3. Normalized effective modulus of the piezoelectric stack shunted with two types of hybrid circuits: (a) TYPE I circuit; (b) TYPE II circuit.

shunting circuits can be reduced in achieving a much lower effective modulus, which is helpful when building real circuits. However, it has been proved that the piezoelectric material selection will not affect the final performance of the adaptive metamaterial beam. The constitutive material and geometric parameters of the metamaterial beam used for calculations are listed in table 1. Based on equation (10), the complex band structure of the metamaterial beam with short circuits is calculated and shown in figure 2(a). The normalized frequency Ω is defined by ω/ω_0 where ω_0 is the local resonant frequency of the proof mass when the PMN-PT stacks are shorted. For the metamaterial design with parameters given in table 1, the local resonant frequency $(\omega_0/2\pi)$ is analytically determined as 9.60 kHz. In figure 2(a), dispersion relations of evanescent flexural-wave modes are manually removed, and attention is paid to the propagating flexural waves and their attenuations. According to equations (9) and (10), the real part of the wavenumber represents the propagation constant of the flexural wave while the imaginary part of the wavenumber indicates the wave-attenuation constant. As illustrated in figure 2(a), both the real part and the imaginary part of the wavenumber in a wave-attenuation region from $\Omega = 1.0$ to 1.38 (larger shaded area) are not zero due to the biharmonic flexural-wave governing equations, which are different from the longitudinal wave equations. This means that the flexural wave in those frequency components is neither a purely propagating wave nor a purely evanescent wave, and will decay as it propagates along the metamaterial beam. Furthermore, due to the periodic nature of the metamaterial beam, another band gap caused by the Bragg scattering is generated and is found for Ω between 7.82 and 7.98 (smaller shaded area). However, it can be observed from the left-hand side of figure 2(a) that the attenuation ability of the Bragg gap (BG) is much lower compared with that of the resonant gap (RG).

In order to design appropriate hybrid shunting circuits to achieve extremely broadband wave attenuation, the wave band-gap behavior of the metamaterial beam with various effective modulii of the mechanical connectivity is characterized in figure 2(b). In the calculation, the effective modulus of the

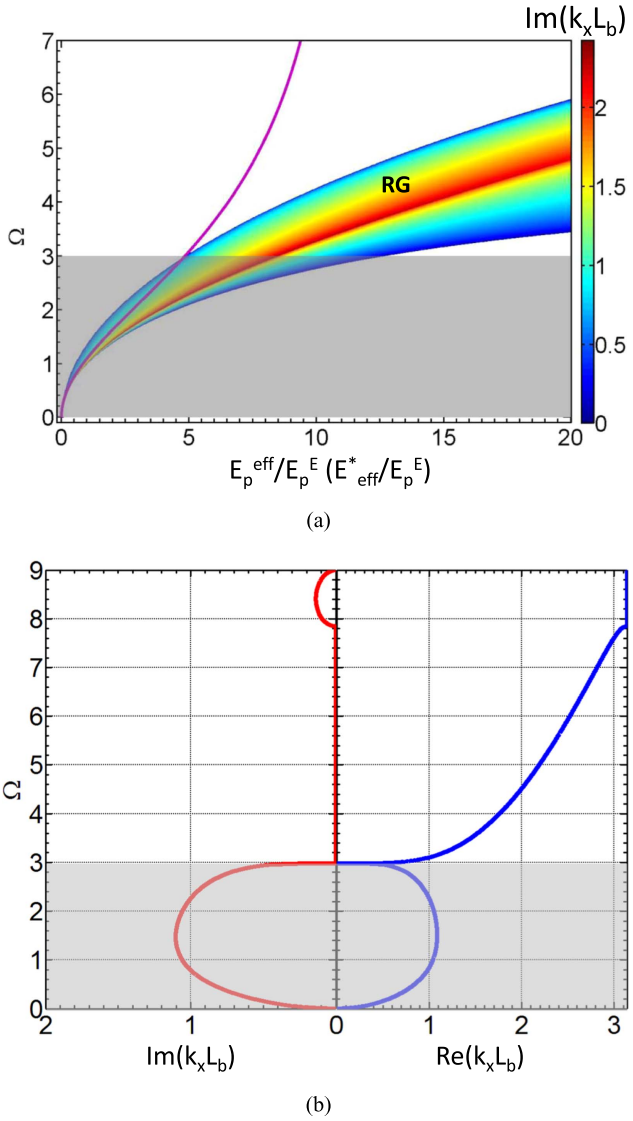

Figure 4. (a) Frequency-dependent normalized effective modulus of the piezoelectric stack, E_p^{eff}/E_p^E, for λ_1 being -1.0 and the normalized band-gap frequency region of the metamaterial beam with different normalized effective modulii of the mechanical connectivity, E_{eff}^*/E_p^E. (b) Complex band structure of the adaptive metamaterial beam with TYPE I circuits.

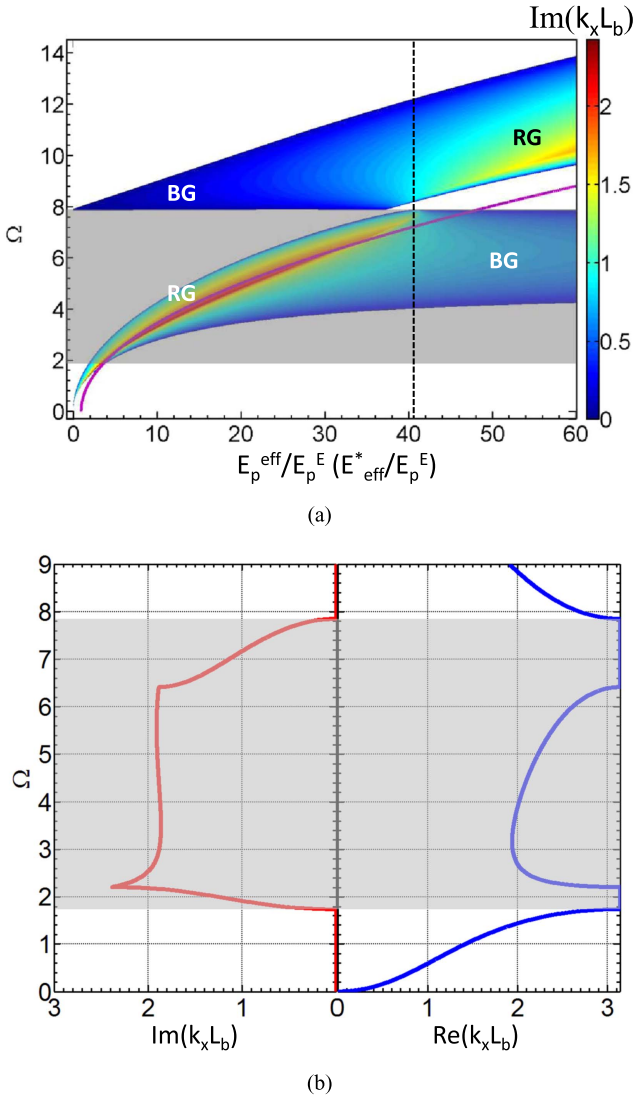

Figure 5. (a) Frequency-dependent normalized effective modulus of the piezoelectric stack, E_p^{eff}/E_p^E, for λ_2 being $-(1 - k_{33}{}^2)$ and the normalized band-gap frequency region of the metamaterial beam with different normalized effective modulii of the mechanical connectivity, E_{eff}^*/E_p^E. (b) Complex band structure of the adaptive metamaterial beam with TYPE II circuits.

mechanical connectivity E_{eff}^* is assumed to be frequency-independent in contrast with the effective modulus of the shunted piezoelectric stack. In the figure, the color legend represents the imaginary part of the normalized wavenumber. It can be observed from the figure that a passing band usually exists between the RG and BG, and the width of this passing band is smallest when the normalized modulus, E_{eff}^*/E_p^E, is around 40. Also shown in the figure, when E_{eff}^*/E_p^E is smaller than 41 (dashed line), the RG is present at lower frequencies than that of the BG. However, if E_{eff}^*/E_p^E is greater than 41, the RG will be present at higher frequencies than the BG. It is shown in the figure that if the normalized modulus, E_{eff}^*/E_p^E, is increased from 0 to 100, the RG can occupy very large frequency regions with Ω from 0 to 16, while the BG is found at frequencies Ω from 4 to 12. This is expected, because the resonant frequency of the proof masses is gradually increased when the effective modulus of the mechanical connectivity increases. In addition, it is noted that the frequency region of the RG is very narrow at lower frequencies when the mechanical connectivity has a smaller modulus, which indicates that it is impossible to achieve broadband low-frequency wave attenuation with frequency-independent modulus control. Therefore, proper frequency-dependent modulus-control algorithms will be employed to achieve broadband wave attenuation in extremely low- and/or high-frequency regions.

3.2. Effective modulus control of the piezoelectric stack by shunting hybrid circuits

According to equations (2) and (3), the effective modulus of the piezoelectric stack with different hybrid circuits is

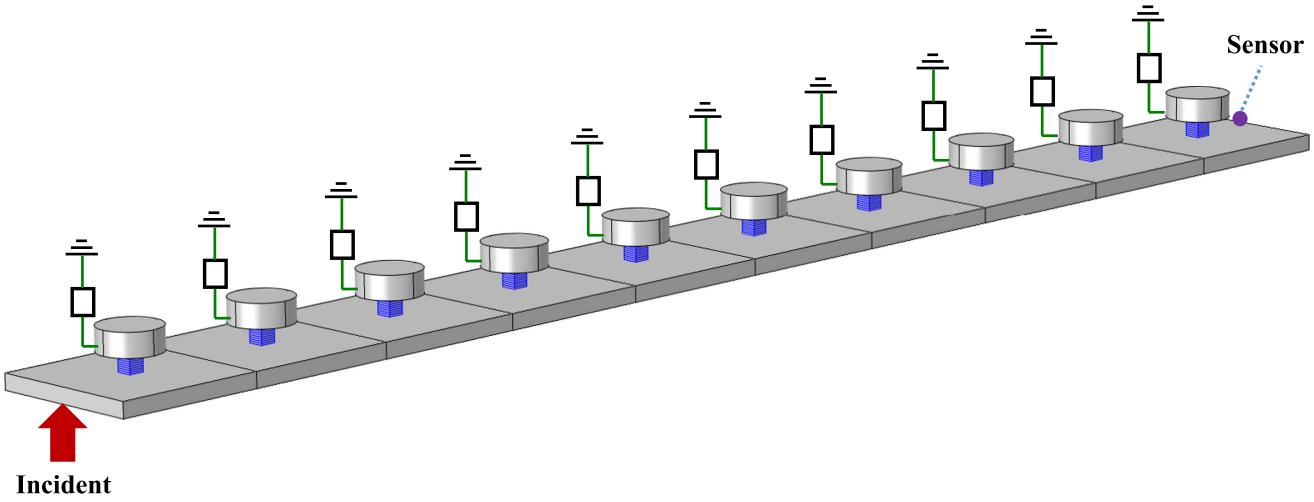

Figure 6. Schematic of numerical simulations of the adaptive metamaterial beam for vibration attenuation.

calculated as a function of different negative capacitances and shown in figures 3(a) and (b) for TYPE I and TYPE II circuits, respectively. In the two figures, the negative inductances are selected to be the same with both ω_{s1} and ω_{s2} being $2.1\pi \times 10^4$ 1/s. As illustrated in figure 3(a), for the hybrid shunting circuit connected in series (TYPE I circuit); generally at lower frequencies ($f < 4$ kHz), the normalized effective modulus, E_p^{eff}/E_p^E, is close to the case where the stack is only shunted with the corresponding negative capacitance. This is due to the impedance of the negative inductance being very small at lower frequencies. However, at higher frequencies ($f > 80$ kHz), the effective modulus is near to the open-circuit case, because the impedance of the negative inductance is very large at higher frequencies. When a small negative capacitance is used (i.e. $\lambda_1 = -0.05$), the normalized effective modulus, E_p^{eff}/E_p^E, shows a resonant behavior (blue solid curve). It should also be noted that this resonant behavior is different from the resonant behavior of a conventional inductance shunting circuit, where the effective modulus is decreased from the short-circuit modulus to a negative value and then jumps to positive infinity and gradually decreases to the open-circuit modulus. For this case, the resonance behaves in an opposite way, where the modulus is always increasing instead of decreasing, due to the anti-resonant circuits. Also shown in the figure, when λ_1 is selected to be -1.0 and -5.0 (green dashed and red dotted curves), the resonance of the normalized effective modulus, E_p^{eff}/E_p^E, will disappear, and the modulus will be monotonously increased to the open-circuit modulus. Specifically, as shown in the inset zoomed-in figure of figure 3(a), it is interesting to note that the normalized effective modulus, E_p^{eff}/E_p^E, can be gradually increased from zero at 0 Hz for the case with λ_1 being -1.0. The shape of this curve is similar to the shape of the wave-attenuation region at extremely low frequencies shown in figure 2(b), which indicates great potential for broadband and extremely low-frequency wave attenuation by shunting these circuits into piezoelectric stacks.

Figure 3(b) shows the normalized effective modulus, E_p^{eff}/E_p^E, controlled by the hybrid shunting circuit connected in parallel (TYPE II circuit). We can see from the figure that the normalized effective modulus is close to the short-circuit modulus at lower frequencies ($f < 4$ kHz). For higher frequencies, however, the normalized effective modulus is close to the case where the stack is only shunted with the corresponding negative capacitance. The resonance behavior of the normalized effective modulus only exists for the circuit with a relatively large negative capacitance ($\lambda_2 = -0.1$). Special attention will be paid to the case when $\lambda_2 = -(1 - k_{33}{}^2)$, where the normalized effective modulus is increased from the short-circuit modulus to positive infinity when the frequency is increased from 0 Hz to infinity. Because of this feature, this particular circuit has great potential for broadband and extremely high-frequency wave attenuation.

3.3. Band-gap control by hybrid shunting circuits

Based on the frequency-dependent modulus tuning of the piezoelectric stack created with the two types of hybrid shunting circuits shown in figures 3(a) and (b), the band-gap control of the adaptive metamaterial beam at extremely low or high broadband frequencies is explored. To quantitatively identify band-gap frequencies of the adaptive metamaterial beam, figure 4(a) shows the frequency-dependent normalized effective modulus of the piezoelectric stack, E_p^{eff}/E_p^E, for λ_1 being -1.0 and the normalized band-gap frequency region of the metamaterial beam with the change of the normalized effective modulus of the mechanical connectivity, $E_{\text{eff}}^*/E_{\text{p}}^E$, which are also plotted in figures 3(a) and 2(b), respectively. As shown in figure 4(a), when the frequency of the normalized effective modulus of the piezoelectric stack, E_p^{eff}/E_p^E, is located within the band-gap frequency region of the passive metamaterial beam, the band-gap behavior of the adaptive metamaterial beam is activated; otherwise the band-gap behavior of the adaptive metamaterial beam is deactivated. By following this criteria, it is easily concluded that the band-gap frequency of the adaptive metamaterial beam is only located at extremely low broadband frequencies ($\Omega = 0 \sim 3.0$ (shaded area)) and the adaptive metamaterial beam will function

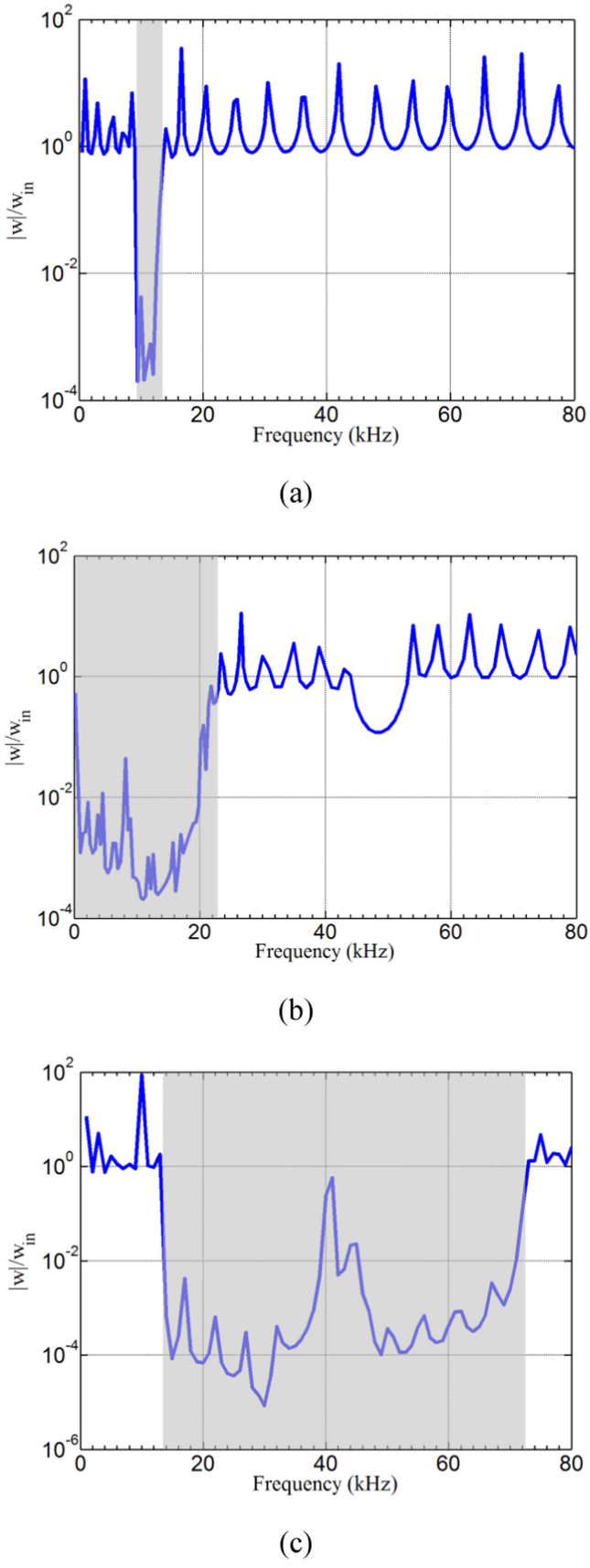

Figure 7. Frequency-response function of the adaptive metamaterial beam: (a) short circuits; (b) TYPE I circuit; (c) TYPE II circuit.

as a conventional high-pass filter. When the normalized frequency Ω is greater than 3.0, no band-gap behavior will be observed in the adaptive metamaterial beam because the frequency of the effective modulus of the piezoelectric stack is out of the band-gap frequency region of the passive metamaterial beam. As also illustrated in figure 4(a), this large wave-attenuation region is caused purely by the RG. In order to validate this broadband wave attenuation, figure 4(b) shows the complex wave-dispersion relations of the adaptive metamaterial beam shunted with the proposed TYPE I circuits. In the figure, material and geometric parameters are unchanged with those in figure 4(a). As expected, the positive imaginary part of the normalized wavenumber (attenuation constant) occupies the lower frequency region of Ω from 0 to 3.0 (shaded area), which coincides exactly with the predication in figure 4(a). Furthermore, both the real and imaginary parts of the wavenumber are half-circular shapes in the wave-attenuation region. It can be concluded that flexural waves with lower frequency components ($\Omega < 3.0$) can be completely attenuated. Therefore, the adaptive metamaterial beam with a TYPE I circuit can be proposed as a high-pass flexural-wave filter.

Figure 5(a) shows the frequency-dependent normalized effective modulus of the piezoelectric stack, E_p^{eff}/E_p^E, for λ_2 being $-(1 - k_{33}{}^2)$ and the normalized band-gap frequency region of the metamaterial beam with the change of the normalized effective modulus of the mechanical connectivity, E_{eff}^*/E_p^E, which are also plotted in figures 3(b) and 2(b), respectively. As shown in the figure, the effective modulus of the piezoelectric stack is located within the band-gap frequency region of the passive metamaterial beam when Ω is between 1.8 and 7.8 (shaded area), which indicates an extremely large wave-attenuation region at relatively high frequencies. Therefore, the adaptive metamaterial beam can function as a low-pass filter at a subwavelength scale. Similar to figure 4(b), 5(b) shows the complex wave-dispersion relations of the adaptive metamaterial beam with TYPE II shunting circuits by using the same material and geometric parameters as those used in figure 5(a). As shown in the figure, the band-gap frequencies are identical with those predicted in figure 5(a). Furthermore, the attenuation constant (imaginary part of the wavenumber) is relatively uniform in the band-gap frequency region (shaded area) and the attenuation ability is found to be stronger than that for lower frequency waves, shown in figure 4(b). In addition, the real part of the wavenumber can be used to illustrate the working mechanisms at different frequencies. For instance, at the beginning and end of the large band gap ($\Omega = 1.8 \sim 2.2$ and $\Omega = 6.4 \sim 7.8$), the normalized real part of the wavenumber is equal to π, which indicates Bragg scattering at these frequencies. At frequencies between these two regions, the wave attenuation is mainly caused by the out-of-phase motions of tunable local resonators. By changing the value of the shunted negative inductance, the

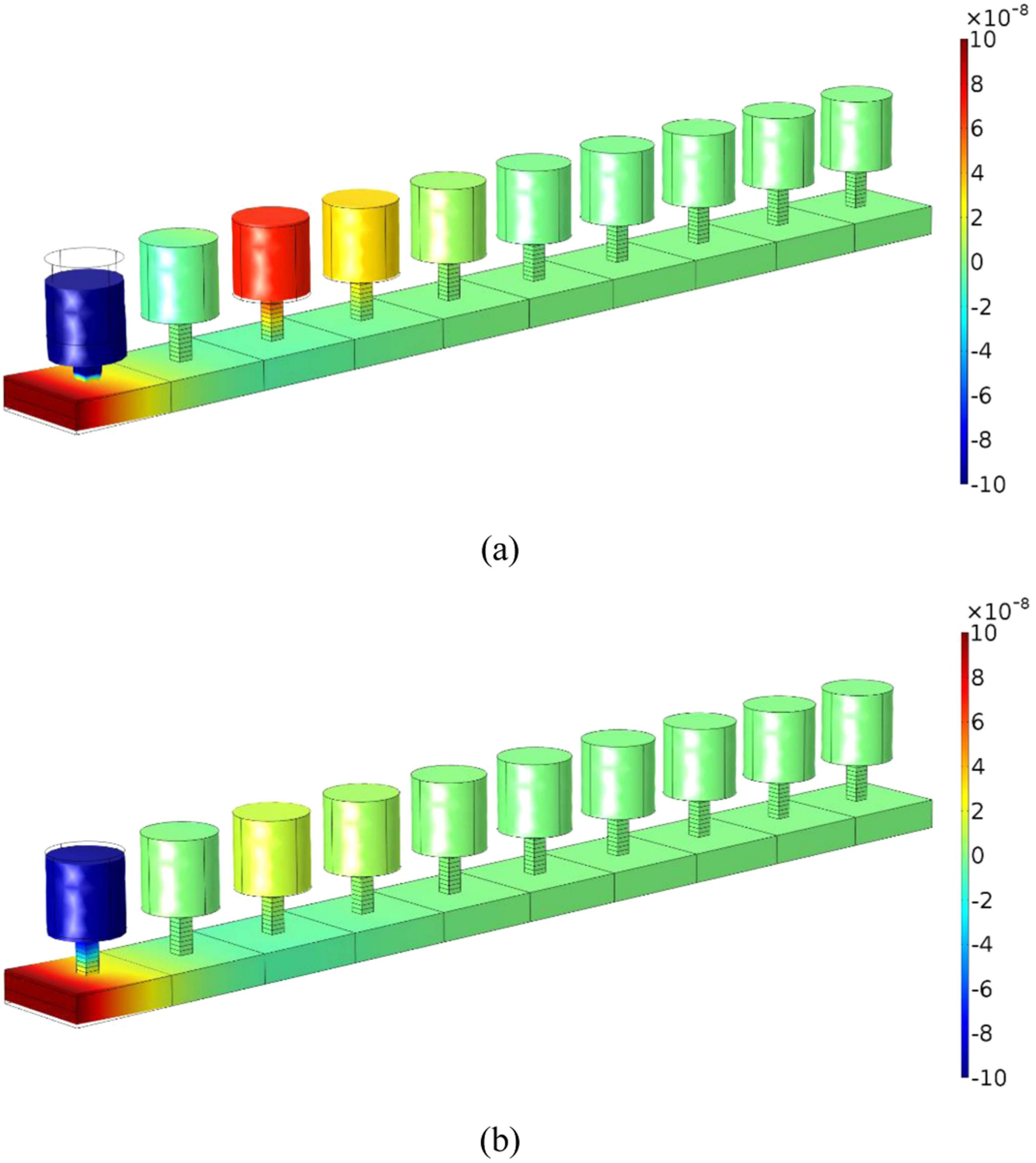

Figure 8. Mode shapes of a finite adaptive metamaterial beam with TYPE I circuits at different frequencies: (a) 5 kHz; (b) 15 kHz.

working mechanism in the higher wave-attenuation frequency region can be altered.

3.4. Numerical demonstrations of wave attenuation in the adaptive metamaterial beam

In order to examine the performance of the adaptive metamaterial beam with hybrid shunting circuits for extremely broadband low- and high-frequency wave attenuation, numerical simulations of wave attenuation with ten adaptive metamaterial unit cells are conducted. A schematic of these studies is shown in figure 6. In the figure, a time harmonic out-of-plane displacement field, $w_{in}e^{i\omega t}$, is prescribed on the left-hand edge of the metamaterial beam. The wave-attenuation properties are examined by measuring the averaged out-of-plane displacement amplitude ratio between the right-hand

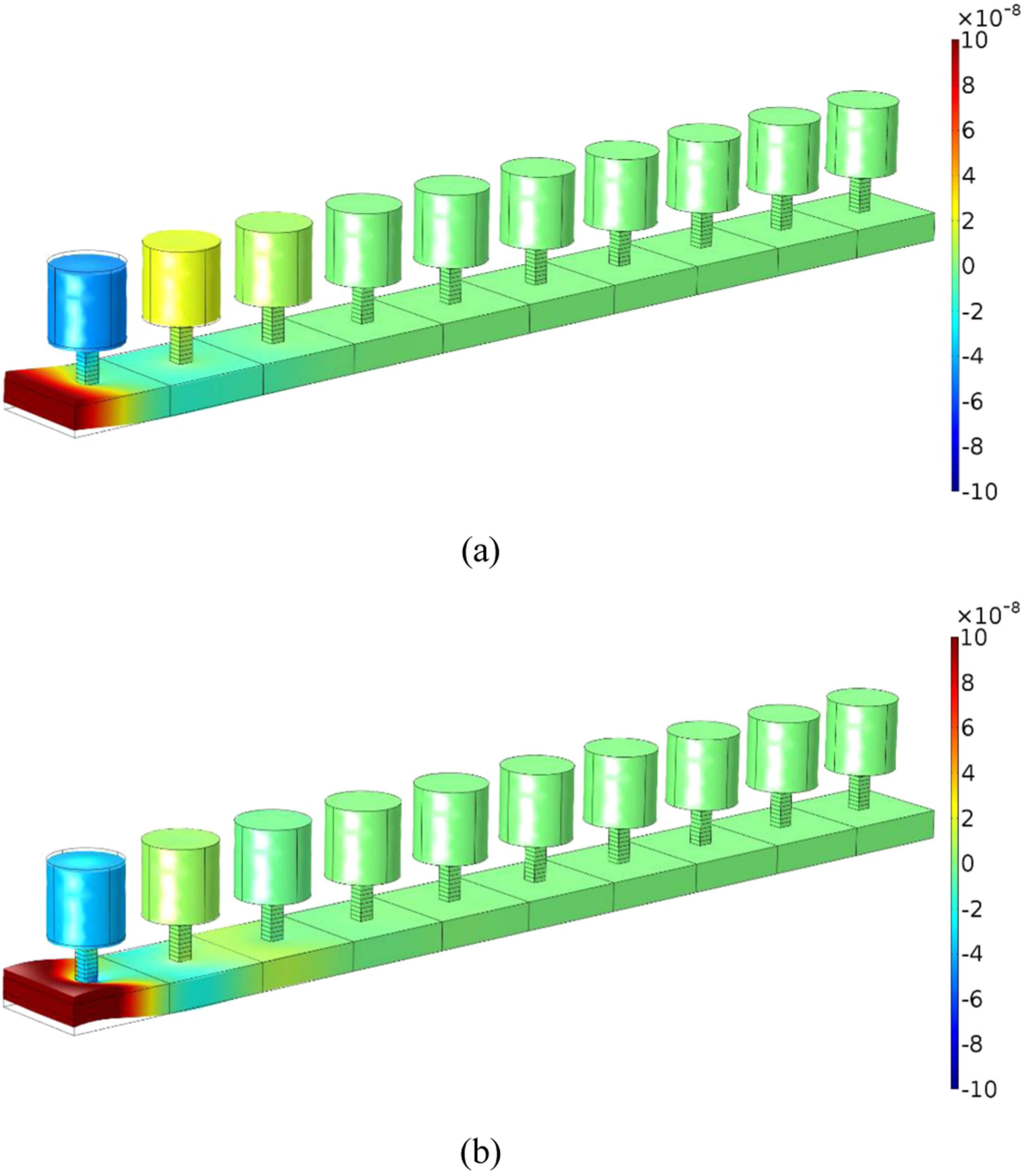

Figure 9. Mode shapes of a finite adaptive metamaterial beam with TYPE II circuits at different frequencies: (a) 30 kHz; (b) 60 kHz.

(denoted as sensor) and left-hand (denoted as incident) edges of the metamaterial beam. A 3D linear piezoelectric theory is applied to the model to describe dynamic behaviors of the shunted piezoelectric stack by using the commercial FE software, COMSOL Multiphysics.

Figure 7(a) shows the frequency-response function of the adaptive metamaterial beam when the piezoelectric stacks are connected with short circuits. In the study, geometric and material parameters are the same as those used in figure 2. Other 3D piezoelectric material parameters of the PMN-33%PT are given in table 1. As illustrated in the figure, a single narrow transmission dip is observed at frequencies between 9.4 kHz and 13.6 kHz (shaded area), due to out-of-phase resonant motions of proof masses. This

wave-attenuation region is in good agreement with the band-gap frequencies predicted by the analytical dispersion relations shown in figure 2(a). Figures 7(b) and (c) show the frequency-response functions of the adaptive metamaterial beam shunted with TYPE I and TYPE II circuit designs, respectively. In our 3D simulations, all of the boundary effects are considered. For example, the top and bottom surfaces of the piezoelectric stacks are assumed to be perfectly bonded to the host beam and proof masses, which will induce in-plane constraints on the PMN-PT stacks. Therefore, the transverse and longitudinal modes of the piezoelectric material will be coupled with each another. In order to achieve the desired performance demonstrated in figures 4(b) and 5(b), the shunted negative capacitance needs to be modified slightly. Specifically, for the TYPE I circuit, λ_1 is selected as -0.971. As shown in figure 7(b), the frequency-response function of the adaptive metamaterial beam with TYPE I circuits demonstrates the desired broadband low-frequency vibration attenuation from 0 to 23.0 kHz (shaded area), which agrees well with theoretical predictions shown in figure 4(b). To demonstrate the wave-attenuation mechanism, the mode shapes of the adaptive metamaterial beam at 5 and 15 kHz are shown in figure 8(a) and (b), respectively. It can be found that the flexural wave can be efficiently attenuated by the out-of-phase motions in the designed resonators, in which the dominated motion along the z-direction is displayed. Furthermore, for the metamaterial beam with TYPE II circuits, λ_2 is selected as -0.1535 in the simulations. As expected, an extremely broadband high-frequency vibration-attenuation region with frequencies from 13.5 to 73.0 kHz is observed in figure 7(c) (shaded area), which is almost identical with that shown in figure 5(b) found using the theoretical approach. In addition, the mode shapes of the adaptive metamaterial beam with TYPE II circuits at 30 and 60 kHz are shown in figure 9(a) and (b), respectively. Similar to those illustrated in figure 8, efficient wave-attenuation at higher frequencies with TYPE II circuits can be observed in figure 9. It should be noted that a transmission peak exists inside the broadband transmission dip, which is caused by the rotational motions of proof masses. In the future, geometric optimizations will still be needed in order to reduce or eliminate the rotational mode and obtain greater attenuation performance.

4. Conclusions

In this paper, we present a novel approach to achieve extremely broadband flexural-wave/vibration attenuation based on tunable local resonators made of piezoelectric stacks shunted by hybrid negative-capacitance and negative-inductance circuits. First, wave-dispersion relations of the adaptive metamaterial beam are calculated analytically by using the TM method. The unique modulus tuning properties induced by the hybrid shunting circuits are then characterized conceptually, from which the frequency-dependent modulus tuning curves of the piezoelectric stack located within wave-attenuation frequency regions are quantitatively identified. As an example, a flexural-wave high-pass band filter with a wave-attenuation region from 0 to 23.0 kHz is demonstrated analytically and numerically by using the TYPE I circuit, in which the two electric components are connected in series. By changing the connection pattern to be parallel (TYPE II circuit), another super-wide wave-attenuation region from 13.5 to 73.0 kHz is demonstrated to function as a low-pass filter at a subwavelength scale. In general, the proposed adaptive metamaterial design is different from the previous active metamaterial design with frequency-independent modulus tuning. The proposed adaptive metamaterial possesses a super-wide band-gap created both naturally and artificially. Therefore, it can be used for the transient wave mitigation at extremely broadband frequencies such as blast or impact loadings. It should be noted that this paper only discusses two specific kinds of hybrid circuits and their applications for 1D wave attenuation, although numerous other circuit combinations and wave phenomena are still unexplored.

The employment of adaptive resonators into metamaterial beams or plates can significantly enlarge their applications in flexural-wave manipulations and vibration attenuations which include, but are not limited to, phase manipulation, super-absorption, super-sensing, and one-way propagation. Specifically, for vibration attenuations, the adaptive resonators do not need to be periodically placed. However, the placements on some node points should be avoided. Optimizations of the placement will be needed for specific mode attenuations. It should also be mentioned that the adaptive resonators can be mounted on both sides of the host beam or plate (symmetrically or asymmetrically) to enhance the attenuation performances. One of the most distinct features of the adaptive resonators is that they can be used for the extremely low-frequency wave attenuations with minimum weight increase of the metamaterial due to the tunable frequency-dependent effective modulus of the mechanical connectivity. We envision that the proposed adaptive design may open up many new possibilities in broadband vibration and wave control.

Acknowledgments

This work is supported by the Air Force Office of Scientific Research under Grant No. AF 9550-15-1-0061 with Program Manager Dr Byung-Lip (Les) Lee.

References

[1] Ma G and Sheng P 2016 Acoustic metamaterials: from local resonances to broad horizons *Sci. Adv.* **2** e1501595
[2] Cummer S A, Christensen J and Alù A 2016 Controlling sound with acoustic metamaterials *Nat. Rev. Mater.* **1** 16001
[3] Haberman M and Guild M 2016 Acoustic metamaterials *Phys. Today* **69** 42–8
[4] Oudich M, Assouar M B and Hou Z L 2010 Propagation of acoustic waves and waveguiding in a two-dimensional locally resonant phononic crystal plate *Appl. Phys. Lett.* **97** 193503

[5] Chen Y Y, Huang G L, Zhou X M, Hu G K and Sun C T 2014 Analytical coupled vibroacoustic modeling of membrane-type acoustic metamaterials: membrane model *J. Acoust. Soc. Am.* **136** 969–79
[6] Yu D L, Liu Y Z, Wang G, Zhao H G and Qiu J 2006 Flexural vibration band gaps in Timoshenko beams with locally resonant structures *J. Appl. Phys.* **100** 124901
[7] Chen Y Y, Barnhart M V, Chen J K, Hu G K, Sun C T and Huang G L 2016 Dissipative elastic metamaterials for broadband wave mitigation at subwavelength scale *Compos. Struct.* **136** 358–71
[8] Xiao Y, Wen J H, Yu D L and Wen X S 2013 Flexural wave propagation in beams with periodically attached vibration absorbers: Band-gap behavior and band formation mechanisms *J. Sound Vib.* **332** 867–93
[9] Forward R L 1979 Electronic damping of vibrations in optical structures *J. Appl. Opt.* **18** 690–7
[10] Hagood N W and Flotow A V 1991 Damping of structural vibrations with piezoelectric materials and passive electrical networks *J. Sound Vib.* **146** 243–68
[11] Bergamini A, Delpero T, Simoni L D, Lillo L D, Ruzzene M and Ermanni P 2014 Phononic crystal with adaptive connectivity *Adv. Mater.* **26** 1343–7
[12] Airoldi L and Ruzzene M 2011 Design of tunable acoustic metamaterials through periodic arrays of resonant shunted piezos *New J. Phys.* **13** 113010
[13] Chen S B, Wang G, Wen J H and Wen X S 2013 Wave propagation and attenuation in plates with periodic arrays of shunted piezo-patches *J. Sound Vib.* **332** 1520–32
[14] Casadei F, Delpero T, Bergamini A, Ermanni P and Ruzzene M 2012 Piezoelectric resonator arrays for tunable acoustic waveguides and metamaterials *J. Appl. Phys.* **112** 064902
[15] Wu S Y 1998 Method for multiple mode shunt damping of structural vibration using a single PZT transducer *Proc. SPIE* **3327** 159–68
[16] Beck B S, Cunefare K A, Ruzzene M and Collet M 2011 Experimental analysis of a cantilever beam with a shunted piezoelectric periodic array *J. Intell. Mater. Syst. Struct.* **22** 1177–87
[17] Collet M, Ouisse M and I Chchou M 2012 Structural energy flow optimization through adaptive shunted piezoelectric metacomposites *J. Intell. Mater. Syst. Struct.* **23** 1661
[18] Zhang H, Wen J H, Chen S B, Wang G and Wen X S 2015 Flexural wave band-gaps in phononic metamaterial beam with hybrid shunting circuits *Chin. Phys.* B **24** 036201
[19] Chen Y Y, Huang G L and Sun C T 2014 Band gap control in an active elastic metamaterial with negative capacitance piezoelectric shunting *J. Vib. Acoust.* **136** 061008
[20] Zhu R, Chen Y Y, Barnhart M V, Hu G K, Sun C T and Huang G L 2016 Experimental study of an adaptive elastic metamaterial controlled by electric circuits *Appl. Phys. Lett.* **108** 011905
[21] Cao H, Schmidt V H, Zhang R, Cao W and Luo H 2004 Elastic, piezoelectric, and dielectric properties of 0.58 Pb (Mg 1/3 Nb 2/3) O 3 −0.42 PbTiO 3 single crystal *J. Appl. Phys.* **96** 549–54